The extreme nonlinear optics of gases and femtosecond optical filamentation[a)]

H. M. Milchberg,[b)] Y.-H. Chen, Y.-H. Cheng, N. Jhajj, J. P. Palastro, E. W. Rosenthal, S. Varma, J. K. Wahlstrand, and S. Zahedpour

Institute for Research in Electronics and Applied Physics, University of Maryland, College Park, Maryland 20742, USA

Under certain conditions, powerful ultrashort laser pulses can form greatly extended, propagating filaments of concentrated high intensity in gases, leaving behind a very long trail of plasma. Such filaments can be much longer than the longitudinal scale over which a laser beam typically diverges by diffraction, with possible applications ranging from laser-guided electrical discharges to high power laser propagation in the atmosphere. Understanding in detail the microscopic processes leading to filamentation requires ultrafast measurements of the strong field nonlinear response of gas phase atoms and molecules, including absolute measurements of nonlinear laser-induced polarization and high field ionization. Such measurements enable the assessment of filamentation models and make possible the design of experiments pursuing applications. In this paper, we review filamentation in gases and some applications, and discuss results from diagnostics developed at Maryland for ultrafast measurements of laser-gas interactions. © *2014 AIP Publishing LLC.*
[http://dx.doi.org/10.1063/1.4896722]

I. INTRODUCTION

The filamentation of intense femtosecond laser pulses in transparent solid, liquid, and gas media is an area of expanding research activity.[1] It has promise for exciting applications and involves examination of fundamental nonlinear optical physics.[1–3] This paper will focus on filamentation in gases, with emphasis on experiments at the University of Maryland. The filament formation process is initiated when the electric field strength of a propagating laser pulse is large enough to induce a nonlinear response in the gas's constituent atoms or molecules, leading to an ensemble-averaged dipole moment nonlinearly increasing with field strength. This nonlinear refractive index perturbation propagates with the pulse as a self-lens. Once the laser pulse peak power, for a Gaussian beam, exceeds a critical value, $P > P_{cr} = 3.77\lambda^2/8\pi n_0 n_2 \sim 2\text{–}10\,\text{GW}$ in gases,[1,4,5] the self-induced lens overcomes diffraction and focuses the beam, leading to plasma generation when the gas ionization intensity threshold is exceeded. Here, λ is the laser central wavelength, n_0 is the unperturbed gas refractive index, and n_2 is the nonlinear index of refraction, defined in Gaussian units by $n_2 = 12\pi^2\chi^{(3)}/n_0^2 c$, where $\chi^{(3)}$ is the third order nonlinear scalar susceptibility of the medium.[4]

According to the "standard model" of filamentation (more on that later), the on-axis concentration of free electrons then defocuses the beam, and the dynamic interplay between self-focusing and defocusing leads to self-sustained propagation of a tightly radially confined high intensity region (the "core") accompanied by electron density tracks over distances greatly exceeding the optical Rayleigh range corresponding to the core diameter. The tracks can extend

from millimeters to hundreds of meters, depending on the medium and laser parameters. The phenomenon is ubiquitous for femtosecond pulses at the millijoule level in gases and at the microjoule level in liquids and solids,[1] where $P_{cr} \sim 10\,\text{MW}$. "Filament" describes both the extended propagation of the intense optical core and the residual plasma density track, which are typically $\sim 100\,\mu\text{m}$ in diameter.[6] In air, for example, $\lambda = 800\,\text{nm}$ pulses with energy ~ 1 mJ and pulsewidth ~ 100 fs can typically be induced to form single filaments with a clean and well-defined transverse density profile, as this laser peak power is not too in excess of P_{cr}. Pulses with peak powers beyond several P_{cr} tend to form multiple filaments owing to the transverse modulational instability,[1] with filament transverse locations that can vary shot-to-shot.

The filamentation of a femtosecond pulse can be viewed as occurring on a temporal slice-by-slice basis. Time slices early in the pulse envelope must propagate longer distances before they accumulate sufficient nonlinear phase front curvature to overcome diffraction and collapse, ionizing the gas and then refracting, whereas later time slices near the peak of the pulse envelope propagate shorter distances before collapse, ionization, and refraction. The overall effect by the full pulse envelope is a tight high intensity core of laser light and generated plasma, surrounded by a less intense reservoir of nonlinear-phase-shifting light, which is both converging on the core from self-focusing and diverging from it owing to refraction from the plasma. These dynamics can result in temporal pulse splitting and axially nonuniform plasma channels.[6–8]

This paper is organized as follows. Section II briefly reviews some applications of femtosecond filaments. It is by no means comprehensive but tends toward relatively recent highlights. Section III discusses filament diagnostics, with emphasis on two diagnostics used by our group, ultrashort

---

pulse spatial interferometry, and single shot supercontinuum spectral interferometry (SSSI). These diagnostics have proved crucial in elucidating the ultrafast nonlinear processes underlying femtosecond filamentation and settling a related debate. In Sec. IV, we review this debate and discuss the role our measurements have played in it. Section V briefly covers recent efforts to extend the length of filaments. Finally, Sec. VI reviews the post-filament gas dynamics induced by the nonlinear energy deposition and discusses applications of the gas response.

II. FILAMENT APPLICATIONS

One of the more spectacular effects accompanying filamentation is supercontinuum (SC) generation, a coherent, ultra-broadband optical beam co-propagating with the filament,[9,10] resulting from ultrafast nonlinear phase evolution of the pulse as it propagates through the fast material response it induces in the medium. This light can be used for filament-based white light LIDAR of the atmosphere from filamentation at large distance scales[11] or generated by filamentation in sealed gas cells, where it can be accompanied by self-compression and spatial mode cleaning of the filamenting pulse.[10]

The long ionization tracks left by filaments have stimulated work in guided high voltage discharges,[12] and the related dream of laser filament-guided atmospheric lightning.[13] However, both the low electron density in typical extended filaments ($<$few $10^{16} \, \text{cm}^{-3}$ (Ref. 6)) and the nanosecond plasma lifetime[14] have made filament-guided discharges much longer than $\sim 1 \, \text{m}$ difficult. Even at a meter length, such discharges had not been reproducible or uniform. Recently, meter long, uniform discharges in air sustained by a compact low jitter Tesla coil have been generated.[15] The same group has demonstrated that laser filaments can coax high voltage discharges to occur far from their normal path, even forcing them to follow right angle paths in free space.[16] Even longer discharges await a more continuous filament with a higher and much longer-lived electron density. Femtosecond filaments in gases are a burgeoning source of coherent THz radiation with clear advantages over other laser-driven sources in biased semiconductors or nonlinear crystals. Most importantly, filaments allow very high pump pulse intensities without permanent material damage. The free electron current generated during laser ionization and driven by the pulse envelope is in fact the primary THz source.[17] Filaments also allow generation of THz at locations distant from the source, an important feature for applications such as remote sensing of complex molecules. THz generation in filaments is becoming increasingly finely controlled. Complex control of the THz polarization state has been demonstrated using external electrodes to modify the laser-driven electron trajectories in the filament plasma,[18] and the detailed THz waveform has been controlled by the carrier envelope phase of the filamenting pulse.[19] THz generation in filaments by 2-color laser fields (typically the fundamental and second harmonic of Ti:Sapphire) has been found to be especially efficient, allowing even stronger laser envelope-driven electron currents. Despite the gains, THz yields are still low, with laser-to-THz

conversion efficiencies of $\sim 10^{-4}$–10^{-3}. Recently, phase matching in 2-color filament-based THz generation has been demonstrated,[20] with the yield scaling linearly with plasma length, suggesting that further extending filaments is a promising scheme for THz generation.

Another concept for radiation generation at a distance, to be used for remote sensing applications, is filament-initiated atmospheric backward lasing, with schemes for both O_2 (in the near-infrared)[21] and N_2 (in the ultraviolet).[22] A filament-pumped backward-directed laser would enable probing of the intervening atmosphere. Some N_2 schemes are based on two pulses: the filament pulse weakly ionizes the air to $\sim 10^{16} \, \text{cm}^{-3}$, and then a co-propagating "heater" pulse heats these electrons, which then pump the molecular transition, with preliminary experiments using a $\lambda = 0.8 \, \mu\text{m}$ filament and a $\lambda = 1.064 \, \mu\text{m}$ heater pulse.[23] Meanwhile, backward N_2 lasing has been demonstrated in a high pressure (6 atm) N_2/Ar gas cell driven only by a $\lambda = 3.9 \, \mu\text{m}$ laser pulse,[24] with the laser transition upper state populated via a different mechanism than in Ref. 22. A different remote sensing approach, with molecular specificity, has been achieved by exploiting the extreme bandwidths and short pulses generated in filaments to impulsively pump characteristic vibrational states and then probe them with a narrower bandwidth, non-filamenting pulse to generate a stimulated Raman spectrum for analysis.[25] The same group also directly measured the extreme optical pulse shortening, which takes place inside a filament core.[26]

Since the first demonstration of femtosecond filamentation in air,[27] filaments typically have been generated using millijoule-level $\lambda = 0.8 \, \mu\text{m}$ pulses of duration $\sim 100 \, \text{fs}$ from Ti:Sapphire lasers. Recently, the development of new high power mid-infrared (MIR) laser sources have made possible the generation of filaments using $\lambda = 3.9 \, \mu\text{m}$.[28] Since $P_{cr} \propto \lambda^2/N$, where N is the atomic/molecular density of the propagation medium, at 1 atm this scaling demands MIR pulse energy exceeding the laser output. A high pressure gas cell was used to decrease P_{cr} to allow filamentation with 7 mJ pulses. Supercontinuum generation from these MIR filaments produced spectra spanning an enormous range, $0.35 \, \mu\text{m}$–$5 \, \mu\text{m}$. At a fixed gas density, an advantage of MIR over $\lambda = 0.8 \, \mu\text{m}$ filaments for some applications is lower electron density, a wider diameter core, and longer propagation distances. These features were crucial in recent experiments where the same MIR laser driver, propagating in a hollow high pressure gas-filled capillary, generated coherent high harmonic radiation up to 1.6 keV.[29] Simulations indicate that filamentary propagation inside the capillary is responsible for spatio-temporal compression and self-confinement of the driver pulse, increasing the conversion efficiency to coherent keV x-rays.

One consequence of femtosecond filamentation only recently investigated is the long time hydrodynamic response of the gas through which the filaments have propagated and nonlinearly deposited energy. The evolving gas response can form long-lived, extended, and robust optical waveguides, with some of the most exciting applications in air. This is covered in Sec. VI below.

III. DIAGNOSTICS OF FILAMENTATION

As discussed above, the offsetting nonlinearities responsible for extended filament core propagation are self-focusing from the bound electron nonlinear response and plasma generation. The approach at the University of Maryland has been to directly measure these nonlinearities to both understand the physical processes involved and to provide input for propagation models, for example, Ref. 30.

A. Measurement of optical nonlinearity at high intensity

1. Single-shot supercontinuum spectral interferometry

The ultrafast optical response of atoms and molecules to short laser pulses manifests itself through changes in the field-induced dipole moment. The ensemble average of the induced dipole response is the transient refractive index of the medium. We use a form of spectral interferometry—SSSI[31–33]—to determine the transient refractive index by measuring, with ~5 fs femtosecond time resolution and ~3 μm space resolution, small transient nonlinear phase shifts imposed on a chirped (frequency-swept) probe pulse. The phase shift is imposed on the weak probe pulse by the fast medium response induced by a strong pump pulse. The phase-shifted probe is interfered with an unperturbed replica pulse (the reference) inside a spectrometer, giving rise to interference fringes in the spectral domain, from which the spectral phase shift is extracted. Provided that the spectral phase and amplitude of the reference pulse is known, one can then extract by Fourier methods the 1D space and time-domain phase shift $\Delta\Phi(x,t) = k\Delta n(x,t)L$ picked up by the probe pulse,[31–33] where k is the probe vacuum wavenumber, $\Delta n(x,t)$ is the transient index shift, x is the transverse dimension across the pumped medium, and L is the axial interaction length. In the geometry used here, strong pump and weak probe and reference pulses propagate collinearly through a thin, flowing gas target, with the reference preceding the pump and the pump temporally overlapped on the probe. A thin target much shorter than the confocal parameter of the pump ensures an axially uniform excitation. See Figure 1. Our technique uses a wide bandwidth (~150 nm) supercontinuum probe pulse, which provides time resolution up to the bandwidth limit of ~5 fs. Because our SC pulse is close to the pump pulse fundamental wavelength of 800 nm, it suffers from much less group velocity walk-off than an alternative pump probe technique using 400 nm pulses.[34] It also has better time resolution because of the broader bandwidth achievable with SC pulses. Unlike transient birefringence techniques for measuring nonlinearities,[35,36] spectral interferometry can measure parallel and perpendicular components of the response independently.[37,38]

The result of the phase extraction is a map of the phase shift as a function of time t and one transverse spatial dimension x, proportional to the index shift as discussed above. Sample results for Ar are shown in Fig. 2, with plots for pump intensity below (left panel) and above (right panel) the ionization threshold of ~80 TW/cm^2.[2] The electronic response of Ar to the laser pulse is instantaneous. This is
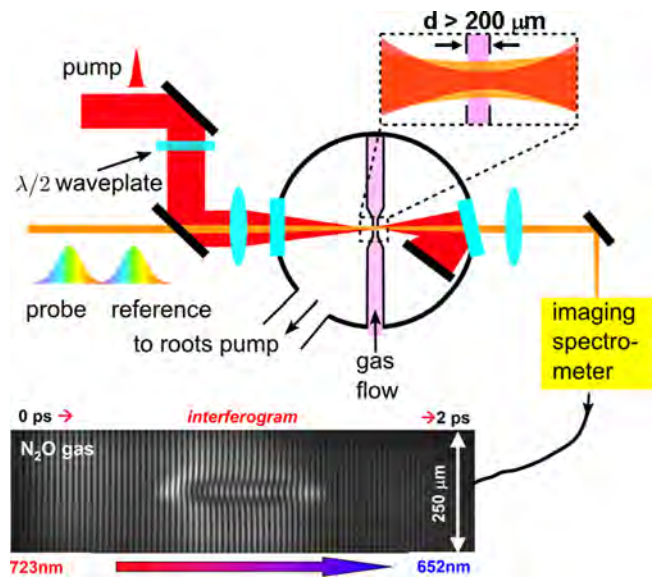

FIG. 1. Experimental setup for SSSI. A pump pulse overlaps with a chirped probe SC pulse in a thin gas flow in a laser-drilled tube in a pumped vacuum chamber. A replica SC reference precedes the pump/probe. The probe and reference interfere in the spectrometer, generating a spectral interferogram (shown), from which the pump-induced time-dependent phase (refractive index) shift in the gas is extracted by Fourier analysis.

because the photon energy (~1.55 eV at $\lambda = 800$ nm) is well below the Ar ionization potential of 15.6 eV, and there are no rotational or vibrational degrees of freedom which provide an inertial response lag. At low intensities (left panel), the nonlinear phase shift follows the pump envelope in space and time, $\Delta\Phi(x,t) \propto \Delta n(x,t) = n_2 I(x,t)$.[2,5,38] At higher intensities, a negative-going signal due to the generated plasma appears (right panel). The transverse spatial width of the plasma signal is narrower because the ionization rate is higher order in the laser field than the second order Kerr response. Free electrons create a negative contribution to the refractive index $\Delta n_{pl} \sim -N_e/(2N_{cr})$, where N_e is the free electron density and N_{cr} is the critical density (the density at which the plasma frequency is equal to the probe optical frequency). Because the polarizability of a free electron is greater than that of a bound electron, the onset of the negative plasma response masks the positive Kerr response and appears to "erode" the central back part of the pulse. After its rapid onset, the plasma signal is constant, as the recombination time is much longer than the ~1 ps time window of the extracted SSSI trace. For a sequence of increasing pump intensities, the ionization rate and plasma density increase as seen in the traces of Fig. 3. The pulse "erosion" effect is seen clearly here: as the peak intensity increases, ionization occurs earlier in the pump temporal envelope with the peak Kerr phase shift moving earlier in time.

SSSI measurements of the nonlinear response of nitrogen gas to variable duration, linearly polarized pump pulses are shown in the top panel of Figure 4. This result is of special interest for atmospheric propagation. The short spike at the beginning of the response for the shortest pump pulses follows the instantaneous electronic Kerr response, while the broader second peak follows the inertial orientational response as the induced dipoles of the diatomic molecular
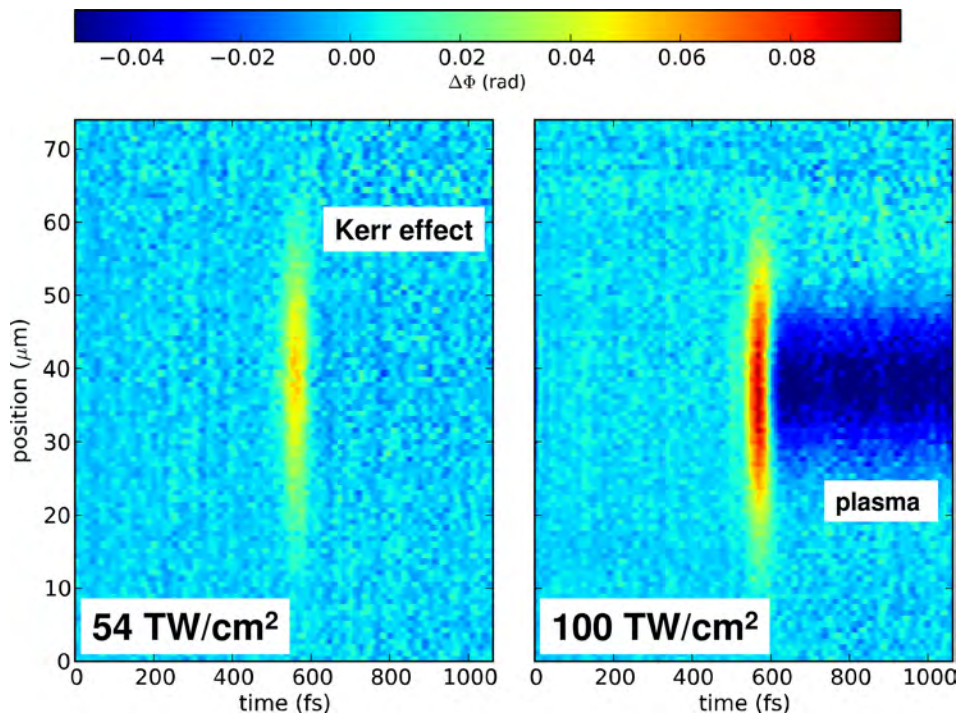
FIG. 2. 2D plots of pump-induced phase shift in 1 atm, 480 μm thick argon flow vs time and transverse dimension. Left panel: Below ionization threshold, Kerr phase shift $\Delta\Phi \propto n_2 I(x,t)$. Right panel: Above ionization threshold, showing positive Kerr signal effectively truncated by onset of ionization.

ensemble are torqued into alignment with the pump pulse polarization. It is clear that for pump pulses $<\sim$80 fs, the instantaneous response dominates; while for longer pulses, the delayed rotational response increasingly contributes. The bottom panel of Fig. 4 shows a calculation of the molecular response, using the equation in the inset, where R is the Raman response function, and n_2 and the molecular polarizability anisotropy $\Delta\alpha$ for nitrogen (included in R) are taken from Ref. 5.

Through spatial interferometry, we are able to measure the optical interaction length $n_0 L$ of our gas sample.[5] This enables absolute measurements of the nonlinear phase shift in target gases as a function of pump laser intensity. Figure 5 shows the nonlinear phase shift induced in noble gases He,

Ne, Ar, Kr, and Xe. Remarkably, the phase shift is linear in the peak laser intensity (quadratic in the field strength) up to the ionization threshold, way beyond the range of applicability of perturbation theory.[2]
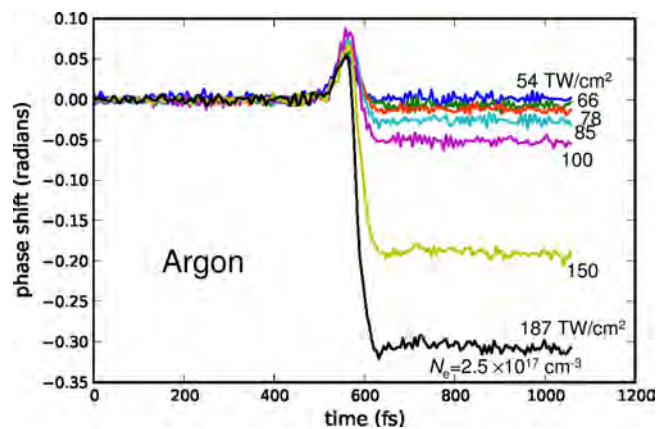

FIG. 3. Sequence of central lineouts of Fig. 2-type plots for pump intensities in the range 54–187 TW/cm² in 1 atm, 480 μm thick argon flow. The positive Kerr shift, which follows the pump envelope at intensities below the ionization threshold, appears to be eroded back in time as pump intensity increases, plasma is generated earlier in the pump envelope, the plasma phase shift increasingly masks the Kerr shift. The electron density produced at the highest intensity is 2.5×10^{17} cm⁻³.
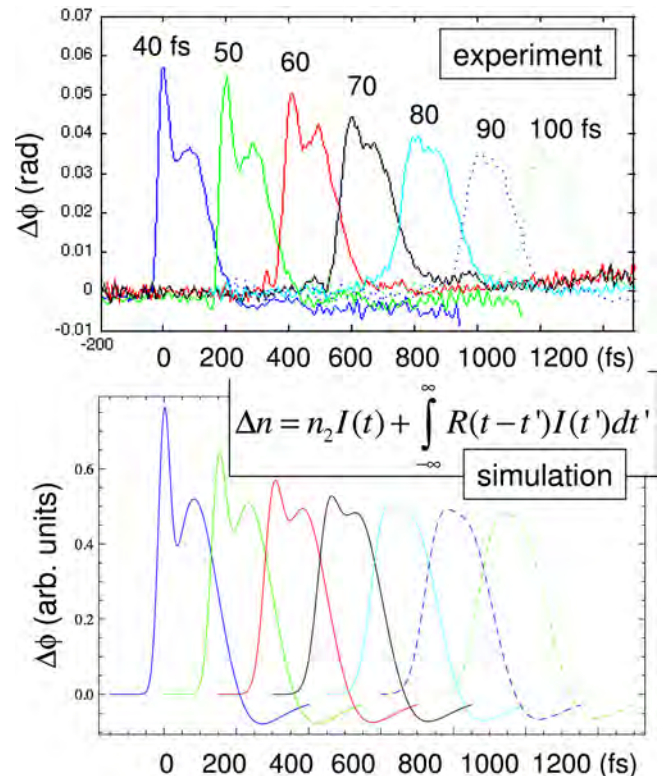

FIG. 4. Pulse width dependence of the nonlinear response in N$_2$ (90 torr). Top panel: Measured phase shift extracted using SSSI, with pump pulse width varied between 40 fs and 100 fs. The pulse energy is kept constant. Bottom panel: Simulated phase shifts for the same pump pulses calculated using inset equation for Δn and the parameters (n_2, $\Delta\alpha$) measured with a 40 fs pulse. Curves are horizontally offset for clarity.
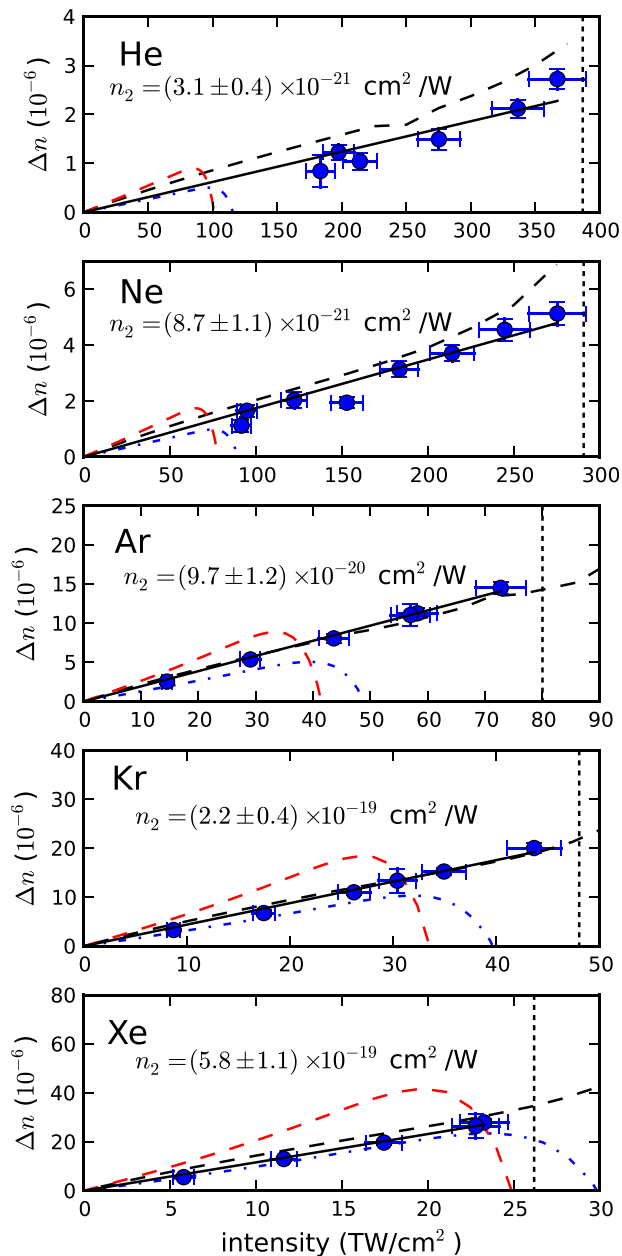
FIG. 5. The nonlinear refractive index Δn of the noble gases experienced by a weak probe pulse as a function of pump laser peak intensity. Blue dots show experimental data points, and the solid line shows a linear fit of the data to $2n_2 I$, the cross-phase modulation shift. Vertical dotted lines show, for each gas, the measured ionization threshold. The red dashed line is the result from Ref. 55. The blue dashed-dotted line is the self-refractive index plotted in Ref. 55. Horizontal error bars denote error in the intensity calibration and vertical error bars denote error in the phase extraction.

B. Measurement of electron density in a femtosecond filament

To fully understand the dynamics of filamentation, it is crucial to determine both laser intensity and electron density in the filament. However, due to the severe distortion of the laser pulse during nonlinear propagation and ionization, complete characterization of spatiotemporal intensity distribution is extremely difficult and such measurements have so far been restricted to filamentation in short water cells.[39] Indirect estimations[40] have shown that the maximum laser

intensity in femtosecond filaments in 1 atm air is clamped at the order of $\sim 10^{13}$ W/cm^2.

On the other hand, numerous attempts have been made to experimentally determine the electron density in the filament, including optical diffraction,[14,40–42] plasma conductance,[43] and seeded breakdown.[8] The measured electron density reported varies by several orders of magnitude, i.e., $N_e \sim 10^{12}$–10^{17} cm^{-3}, and this variation may be caused by (1) different laser and focusing conditions used to generate filaments,[8,14,40–43] and (2) lack of a direct, reliable measurement technique for low-density plasma. The existing methods mentioned above have poor or no spatial resolution and are strongly model-dependent.

Interferometry is a standard tool in experimental plasma physics, and it has been successfully employed in the past to transversely probe the radial and axial distribution of electron density in, for example, plasma channels generated from the line-focus of an axicon[44] or relativistic self-guiding[45] with $N_e > 10^{18}$ cm^{-3}. However, in atmospheric filaments, the electron density, typically $\sim 0.1\%$ of ambient density, is too low to register a phase shift distinguishable from the typical phase front noise in an optical probe beam. To increase the phase sensitivity, we intersect an interferometric probe beam through the filament at a near-grazing angle, which increases the interaction length. While maintaining excellent radial spatial resolution as in the conventional method, the price paid for the small probe crossing angle is reduced axial spatial resolution. However, this is of little concern for meter-scale length filaments. This technique allows measurement of plasma density as low as $10^{14} \sim 10^{15}$ cm^{-3}.

The interferometry setup is shown in Fig. 6. A low energy probe beam with variable time delay is split from the pump beam and counter-propagates at an angle $\theta = 0.75°$ across the filament. It is crucial to use a high-quality probe phase front, which is achieved by a spatial filter. The resolution limit of the interferometer is set by residual phase front noise of $|\delta\Phi_{noise}| \sim 6$ mrad in the probe, which sets the measurable lower bound density to $\sim 5 \times 10^{14}$ cm^{-3}. The plane central to the crossing region is relayed and imaged to a
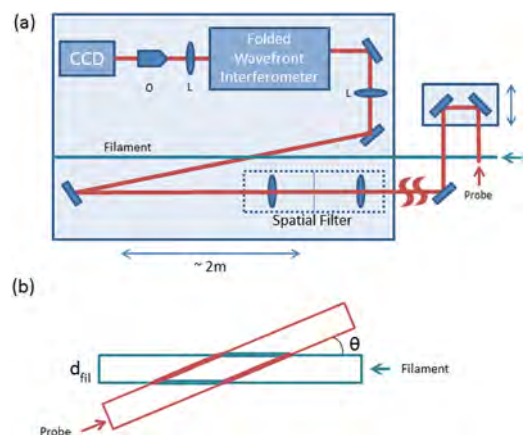

FIG. 6. (a) Interferometry setup, showing imaging lenses (L) and the microscope objective (O). (b) Crossing geometry of probe and filament, with filament width d_{fil} and the crossing angle θ. In (b), the thick red line represents the interaction length of the probe through the filament ($\sim d_{fil}/\sin\theta$), while the thick blue line shows the axial spatial resolution ($\sim d_{fil}/\tan\theta$).

CCD camera by a pair of relay lenses (L) and a microscope objective (O). A folded wavefront interferometer in Mach-Zehnder configuration is installed between the two relay lenses and splits the probe beam into two replicas with variable delays, and nearly collinearly recombines them so that they partially overlap on the CCD camera with slightly different incident angles, forming an interference fringe pattern on the detector chip. The setup is rail-mounted and is translatable along the full filament, which allows sampling of axial locations over a range of 2 m. For the typical measured filament diameters of $d_{fil} \sim 70\,\mu m$, the probe path through the plasma is $d_{probe} \sim d_{fil}/\sin\theta \sim 5\,mm$, and the axial spatial resolution along the filament is $\Delta z_{res} \sim d_{fil}/\tan\theta \sim 5\,mm$. This corresponds to a temporal resolution of $\Delta t_{res} = \Delta z_{res}/c \sim 10\text{--}15\,ps$.

The interferograms are analyzed by standard techniques described in Ref. 44. A sample raw interferogram obtained at ~1 ps probe delay and the corresponding retrieved phase shift image are shown in Figs. 7(a) and 7(b). The phase image in Fig. 7(b) is reminiscent of the middle and left half of a bowtie. The narrowest region in the center represents the tightly imaged section of the filament crossing the object plane of the imaging system, which has a short (~1 mm) depth of field. Due to the pump-probe crossing geometry, approximately 6 cm along the pump propagation direction (z-axis) is projected onto the CCD sensor chip. Because the pump-probe delay is ~1 ps, the pump pulse has propagated only slightly beyond the in-focus region in the center, leaving the right side of the bowtie incomplete. For comparison, another phase image of the filament with much later (~50 ps) probe delay is shown in Fig. 7(c). The local radial electron density profile is extracted from a vertical lineout of the phase shift at the in-focus region at the bowtie centre, using Abel inversion.

The ability to directly measure the electron density with good axial and radial resolution allows a sensitive test of filament propagation physics. Here, we show the results of the electron density measurement for filaments generated in air by two different laser pulse durations, $\tau_{short} = 40$ fs and $\tau_{long} = 120$ fs at a constant peak power $P = 17$ GW, focused at f number $= f_\# = 240$. The interferometer probe delay was set to $\Delta t_{probe} = 1$ ps. The on-axis filament electron density N_e and FWHM diameter d_{fil} as a function of axial position z are shown in Figs. 8(a) and 8(b), where $z = 0$ represents the lens
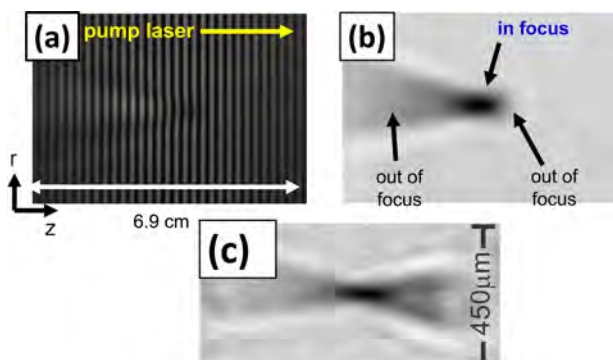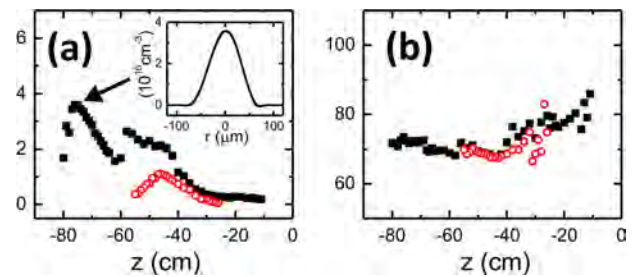

FIG. 8. Axial scan of filament (a) on-axis electron density and (b) transverse FWHM for two pulse durations: $\tau_{short} = 40$ fs (red circles), and $\tau_{long} = 120$ fs (black squares). The pump laser peak power is fixed at P = 17 GW with focusing geometry $f_\# = 240$ ($f = 95$ cm). Each point is a 200-shot average. An electron density radial profile at $z = -8$ cm is shown in the inset in (a). Peak electron densities shown in (a) have 20% uncertainty near the collapse point and 10% over the rest of the filament.

vacuum focus position. A sample electron density radial profile is shown in the inset of Fig. 8(a). For both pulses, d_{fil} is roughly constant over the filament length, except near the end. The axial variation of electron density in the τ_{long} and τ_{short} filaments is quite different: for τ_{long}, the laser pulse experiences stronger self-focusing and collapses more rapidly, i.e., the onset of the filament is closer to the focusing lens. Moreover, the long pulse filament has higher peak electron density and longer overall length. This pulse duration effect originates from the two parts of the optical nonlinearity in air: (1) the nearly instantaneous, electronic response owing to nonlinear distortion of electron orbitals, and (2) the delayed, orientational effect as the induced dipole moment in N_2 and O_2 molecules is torqued toward the laser polarization. As shown in Fig. 4, the orientational effect is dominant for $> \sim 80$ fs pulses. This is consistent with a rotational response timescale of $\Delta t_{rot} \sim T_{rev}/j_{max}(j_{max}+1) \sim 40$ fs, where $j_{max} \sim 20\text{--}30$ for room temperature N_2 in air,[33,46] and T_{rev} is the fundamental molecular rotational period ($T_{rev,N2} = 8.3$ ps for N_2 and $T_{rev,O2} = 11.6$ ps for O_2 (Ref. 47)). Therefore, the filamenting τ_{long} pulse experiences significantly more contribution from the rotational part of the response than the τ_{short} pulse. Also, the secondary electron density peak at $z \sim 5$ cm for τ_{long} is a signature of the delayed molecular response: the leading edge of the τ_{long} pulse is first focused and generates plasma, which defocuses the trailing edge of the pulse. Then the defocused trailing edge in the plasma periphery experiences the leading edge-induced, delayed molecular response and thus is re-focused later, generating the secondary peak of electron density.

IV. FILAMENT PROPAGATION: STANDARD MODEL VS. HIGH ORDER KERR EFFECT

While macroscopic effects of filamentation have been extensively studied over many years, the underlying physical mechanisms were still recently debated. In particular, the laser intensity dependence of the high field bound electron nonlinearity in the major constituents of air (N_2, O_2, and Ar) was revisited in a recent pump-probe measurement.[35,36] It was found that the transient birefringence induced by an intense pump pulse saturated, then became strongly negative at intensities on the order of 30 TW/cm², below the

FIG. 7. (a) A sample interferogram and (b) the retrieved 2D phase image of a filament, at probe delay $\Delta t_{probe} \sim 1$ps. (c) Retrieved phase at $\Delta t_{probe} \sim 50$ ps.

ionization threshold of these gases. This was interpreted as evidence of higher order corrections to the instantaneous Kerr response ("high-order Kerr effect" or HOKE), namely a refractive index $n = n_0 + n_2 I + n_4 I^2 + \ldots$, where n_0 is the unperturbed refractive index, n_2 is the usual Kerr coefficient, and n_i for $i > 2$ are higher-order Kerr coefficients, with $n_4 < 0$, $n_6 > 0$, and $n_8 < 0$, reproducing the observed saturation and negative nonlinear response. This claim has led to a significant controversy about whether such a high order and negative-going Kerr shift exists as a fundamental atomic response to high laser fields. If the nonlinear refractive index became negative at intensities well below the ionization threshold, it would also have an impact on the nonlinear optics of gases over a wide range of wavelengths,[48] enabling plasma-free filamentation,[49,50] "fermionic light,"[51] enhanced harmonic generation,[52] and modifications to self-steepening[53] and conical emission.[54] The effect reported in Refs. 35 and 36 is so strong (i.e., the nonlinearity turns negative at such a low intensity) that it would overturn the so-called "standard model" of femtosecond filamentation as arising from an interplay between self-focusing due to the positive nonlinear polarizability of bound electrons and defocusing from the negative polarizability of the free electrons generated by ionization.[1]

Two of our results presented earlier in this paper constitute a direct assessment of whether such a higher-order Kerr effect is important, and both indicate that it is not. First, we have used SSSI to measure the nonlinear refractive index shift of a wide range of noble gases from lower intensities where perturbation theory is applicable, up to the range of the ionization threshold where perturbation theory should fail. See Figure 5. We found that $\Delta n(x,t) = n_2 I(x,t)$ over the full intensity range with no HOKE corrections needed (the plots of Fig. 5 use peak on-axis intensities). By contrast, the overlaid red and blue dashed curves are predictions using HOKE coefficients,[55] showing the response saturating and going negative at intensities well below the ionization threshold in all cases.

The same measurement technique, SSSI, has also made possible new, accurate measurements of the nonlinear refractive index n_2 and polarizability anisotropy $\Delta\alpha$ for a range of atomic and molecular gases.[5] This is important for realistic propagation simulations.[1,10,30,49,57]

The second result is our direct measurement of the filament electron density profile, shown in Fig. 8. In our $\tau_{short} = 40$ fs filament experiment, the laser parameters are very similar to those used in the simulation of filamentation by Béjot *et al.*,[49] which employs their earlier measured HOKE coefficients[35] to model the nonlinear response of the medium. However, their simulated electron density is more than two orders of magnitude lower than our measurement results. Meanwhile, their comparison simulation,[49] which considers only the Kerr and plasma responses but no HOKE, predicts electron densities in agreement with our measurements. Our conclusion is that the high order Kerr effect, if it exists at all, is too weak to see and has little effect on experiments. In the process of femtosecond filamentation, any negative polarizability needed to offset the nonlinear self-focusing is supplied by free electrons. Our conclusion is that the so-called "standard model" of filamentation is consistent with macroscopic filament behaviour and detailed measurement of the nonlinear response of the gas atoms and molecules.

What was the physics behind the measurements[35] leading to the HOKE debate? An effect not considered was that a plasma grating is formed during temporal overlap of pump and probe beams in that experimental geometry. We have shown that when the pump and probe beams are the same wavelength, as in Ref. 35, this grating coherently scatters light from the pump beam into the probe beam and results in an effective birefringence,[58] explaining all the features of the experiment that led to the HOKE interpretation. This coherent scattering effect is closely related to two-beam coupling,[59] which can transfer energy between pump and probe beams. When a probe of a different color is used, as in our SSSI experiments, the plasma grating is suppressed because the intensity grating then oscillates in time as well as in space. The plasma grating effect fully explains the discrepancy between the transient birefringence experiment[35] and the spectral interferometry experiment.[2,38] Similarly, scattering by the molecular alignment grating fully explains[60] the discrepancy between the values of n_2 measured using each technique.[5,35]

V. ENHANCING FILAMENTATION

One of the important goals for applications of femtosecond filaments is to extend their propagation range. The length of a single filament is constrained by laser energy absorption, which goes into plasma generation and rotational and vibrational excitation (in molecular gases).[61] For ~ 1 mJ pulses, maximum lengths are limited by laser energy loss to $< \sim 5$ m.[62] One recent approach is to use a second laser pulse to augment the filament core's reservoir and thereby provide additional optical energy to resupply the core.[63]

Another concept for lengthening the filament is to exploit the quantum rotational recurrences, which cause quantum beats in the refractive index response of air at standard temperature and pressure.[33,46] By repetitively kicking the molecular rotor with a sequence of pulses spaced at the alignment revival intervals, enhancements in the gas refractive index can compete strongly with the defocusing effect of the plasma to increase and extend the electron density. A preliminary 2-pulse experiment in air has shown enhanced electron density and filament lengthening, as well as optical pulse shaping.[56] Figure 9 shows how the electron density profiles for 2-pulse filaments are sensitive to delay adjustments of the second pulse on a ~ 10 fs time scale. Related simulations[57] for a sequence of 6 appropriately timed pulses show a strong enhancement of electron density and filament length, with "molecular lens" focusing dominating free electron defocusing, with the filamenting pulse quasi-confined as if by a guiding structure.

VI. POST-FILAMENT GAS EVOLUTION

Unique to femtosecond filaments is their extended high intensity propagation over many Rayleigh lengths and their ultrafast nonlinear absorption in the gas, stored in plasma and atomic and molecular excitation.[61] This creates an axially extended impulsive pressure source to drive gas
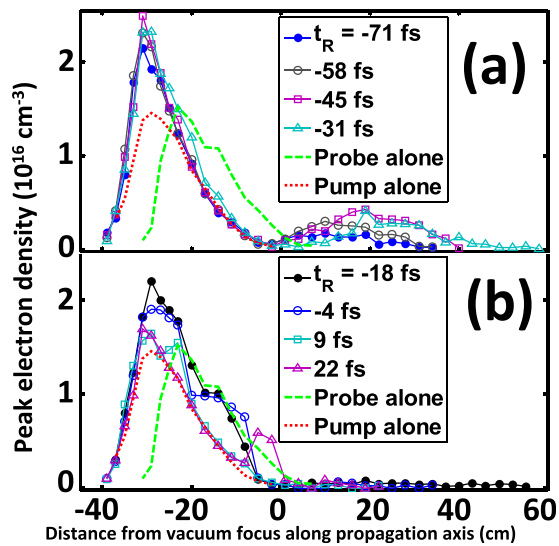
FIG. 9. (a) Electron density at the center of the filament core vs distance relative to the laser vacuum focus. Probe delays are all in advance of the air revival zero crossing at 8.341 ps. (b) Same as (a), except probe delays are closer to and beyond the zero crossing.

hydrodynamics.[61,62,64–66] This initial pressure $P_0(r)$ is determined by repartitioning the initial filament-deposited energy into the thermodynamic degrees of freedom of the neutral gas, $P_0(r) \approx (f_e/f_g)N_e(r)k_B T_e(r) + 2\Delta\varepsilon_{rot}/f_g$, where k_B is Boltzmann's constant, $N_e(r)$ and $T_e(r)$ are the initial electron density and electron temperature profiles immediately after femtosecond filamentation in the gas, f_e and f_g are the number of thermodynamic degrees of freedom of the free electrons and gas molecules, and $\Delta\varepsilon_{rot}$ is the increase in molecular rotational energy density due to the filament. Here, $f_e = 3$, and $f_g = 5$ for air at the typical air heating temperatures ($\Delta T_0 < 200$ K). After the filamenting pulse passes, a gas density depression or hole grows over several hundred nanoseconds. Over the same timescale, a single cycle acoustic wave is launched and by $\sim 1\,\mu s$ has propagated away from the hole. The hole then slowly decays by thermal diffusion over microseconds through milliseconds. This evolution is seen in Fig. 10, which shows interferometrically derived images of the air response to a short filament (top) and a hydrodynamic simulation (bottom).[62,64]

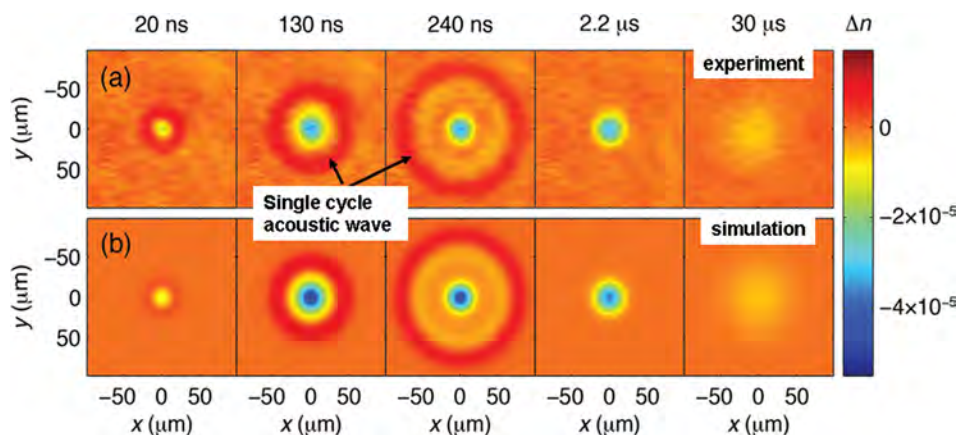Understanding this evolution has led to our use of symmetric filament arrays to generate very long-lived air
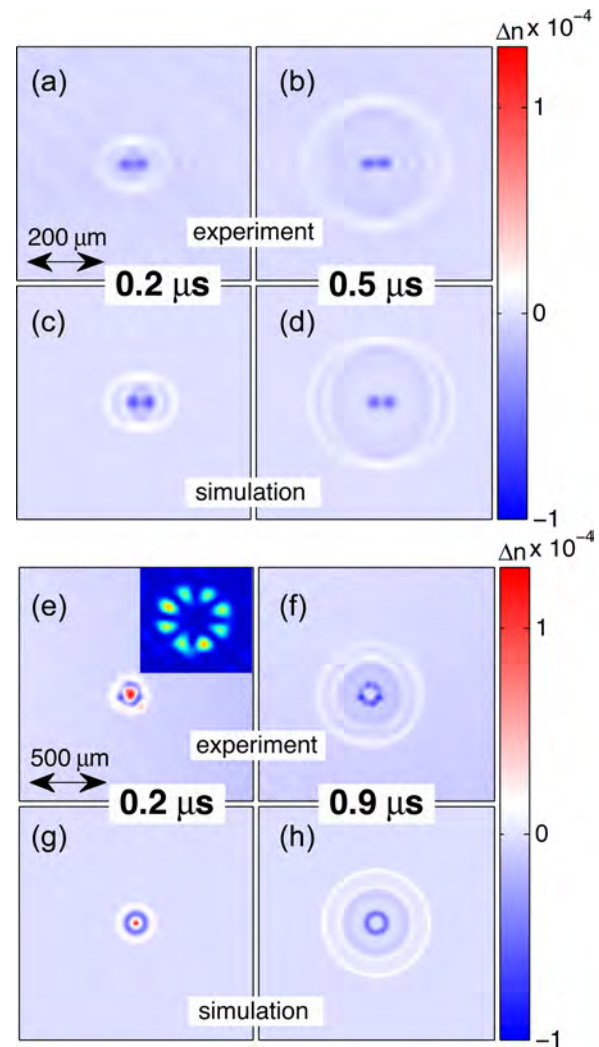

FIG. 11. Interferometrically derived images ((a)–(b)) and simulations ((c)–(d)) of the acoustic response of air to a double filament. Interferometrically derived images ((e)–(f)) and simulations ((g)–(h)) of the acoustic response of air to an 8-lobe filament array. Inset: low intensity focal image of the $LG_{0,\pm4}$ mode used to generate the 8-lobed filament array.

waveguide structures[62] that can support very high power secondary laser pulses. On sub-microsecond timescales, the colliding acoustic waves launched by the filament array form a fiber-like guiding structure with a gas density (or refractive index) enhancement in the centre.[62,66] On timescales well past the acoustic response, the residual gas density holes
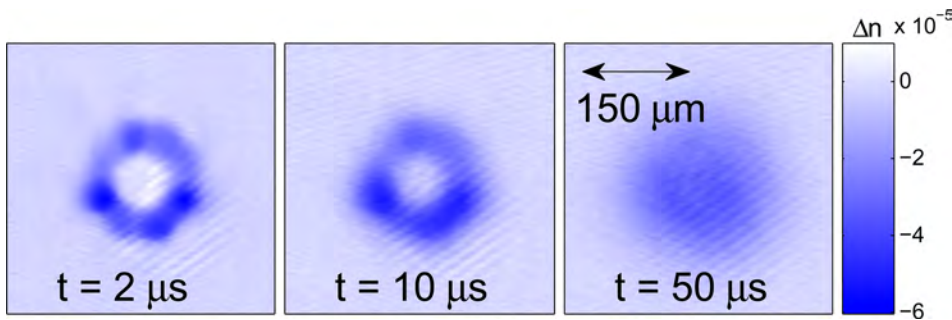

FIG. 10. Interferometric images (top) and simulations (bottom) of the air refractive index (gas density) response to a single filament.

thermally relax and spread over milliseconds, forming the cladding of a long lived fiber-like structure with higher gas density in the center. Figure 11 shows some of the air density (refractive index) structures generated by 2- and 8-filament arrays, where the upper panels ((a), (b), (e), and (f)) are interferometrically derived images, and the lower panels are hydrodynamic simulations. Panels (a) and (b) and their simulations in (c) and (d) show the response induced by a double filament, created by the collapse of a TEM_{01}-like mode, which is produced by inducing a π phase shift between the top and bottom halves of a pre-focused femtosecond pulse using a "half-pellicle."[62,66] Shown are the single cycle sound waves launched by each filament.

Panels (e) and (f) and their simulations in (g) and (h) show the acoustic response to an 8-filament array, formed from the filamentary collapse of a Laguerre-Gaussian $LG_{0,\pm4}$–like beam (shown in the inset). Panel (e) shows the on-axis collision of acoustic waves launched by each of the 8 filaments; such a structure forms an air waveguide in the "acoustic regime."[62,66] The double acoustic wave seen in panel (f) results from the radially inward- and outward-directed waves launched from the 8 filament locations: the inward waves pass through the central axis and collide, reemerging to follow the originally outward-directed waves, all of which superpose into rings. Panels (g) and (h) are from a hydrodynamic simulation assuming that the initial pressure source is a continuous ring; it is seen to model well the air response to 8 discrete filaments.

At longer times $> \sim 1\,\mu s$ after the acoustic wave has propagated away, a ring-shaped density trough is left with ambient, higher density air both in the ring center and outside. The trough is the dark ring in the centre of the image in Fig. 11(f). Figure 12 shows an expanded view of this region for several time delays. This structure can serve as a long-lived optical waveguide in the "thermal regime" capable of guiding very large average powers.[62] For short filaments used for low probe distortion interferometry measurements, the focal features are of reduced transverse scale and dissipate by thermal diffusion over tens of microseconds. For the larger transverse structures characteristic of long filaments, dissipation occurs over milliseconds.[62]

Recently, we have demonstrated that a sequence of properly timed non-ionizing pulses can heat a molecular gas more strongly than can the plasma from a femtosecond filament.[61] A train of four co-propagating, non-ionizing pulses was focused in a chamber backfilled with nitrogen. The long timescale $(40\,\mu s)$ gas density hole depth induced by pulse train heating is proportional to the initial laser energy deposited in rotational excitation of the gas,[61] allowing us to use the interferometrically determined hole depth as a measure of gas heating. The top panel of Fig. 13 shows the four-pulse sequence with computer-controlled delays t_1 and t_2. The $\sim 100\,fs$ pulses had peak intensities 61, 41, 41, and
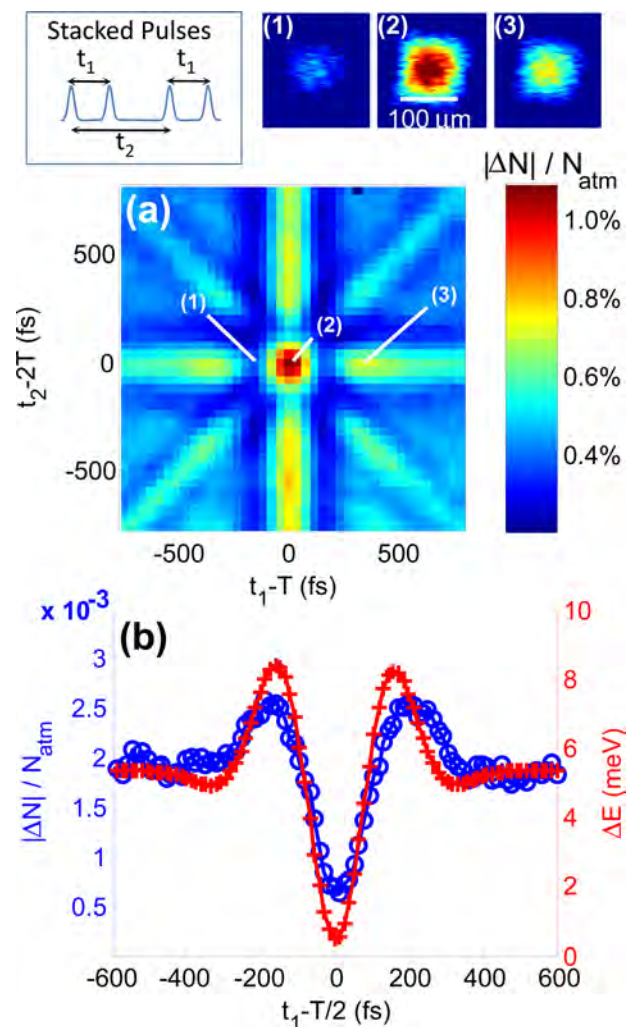

FIG. 13. Interferometric measurement of long timescale density hole for (a) Excitation of rotational states using a train of four non-ionizing laser pulses separated by variable time delays t_1 and t_2 as shown in the inset. Each point in the plot corresponds to maximum density change at the center of the induced density hole. (b) Coherent de-excitation of rotational states results in heating suppression (reduced hole depth). Blue curve (circles): results of the interferometric measurements. Red curve (crosses): density matrix simulation of average rotational energy per molecule.

51 TW/cm^2. Figure 13(a) is a 2D plot showing measured peak hole depth as a function of t_1 and t_2. The maximum hole depth (greatest heating) at $(t_1, t_2) = (0,0)$ corresponds to pulses delayed by a rotational revival period $T = 8.36$ ps, resulting in resonant rotational kicking of the molecular rotors. Other features in the plot—the horizontal, vertical and diagonal stripes– can be understood as resonances involving fewer pulses.[61] Panels (1)–(3) show examples of 2D density hole profiles for several different pulse sequences, illustrating the strong effect of pulse relative timing on the gas hydrodynamics.

In a second demonstration, we showed that pulse sequences not only control heating of a molecular gas but also control heating suppression. Here, a two-pulse sequence was focused into the chamber, with delay varied near the half-revival time $T/2 = 4.16$ ps. The first pulse impulsively excites a rotational wave packet ensemble. The second pulse coherently de-excites the ensemble before collisions cause loss of phase coherence and thermalization. In Fig. 13(b), the blue curve shows the measured peak hole density versus two-pulse relative delay and the red curve is from a density matrix simulation calculating the average energy absorbed per molecule. In essence, energy from the first pulse invested in the wave packet ensemble is coherently restored to the second pulse when the delay is a half-revival time. These results open up the possibility for fine ionization-free control of remote atmospheric density profiles.

VII. CONCLUSIONS

This paper has presented an overview of some of the physics of femtosecond laser pulse filamentation in gases, along with brief discussions of applications, diagnostics developed at the University of Maryland, and implications of the fundamental measurements thus enabled.

ACKNOWLEDGMENTS

[1]A. Couairon and A. Mysyrowicz, Phys. Rep. **441**, 47–189 (2007), and references therein.

[2]J. K. Wahlstrand, Y.-H. Cheng, and H. M. Milchberg, Phys. Rev. Lett. **109**, 113904 (2012).

[3]P. Béjot, E. Cormier, E. Hertz, B. Lavorel, J. Kasparian, J.-P. Wolf, and O. Faucher, Phys. Rev. Lett. **110**, 043902 (2013).

[4]R. W. Boyd, *Nonlinear Optics*, 3rd ed. (Academic Press, 2008).

[5]J. K. Wahlstrand, Y.-H. Cheng, and H. M. Milchberg, Phys. Rev. A **85**, 043820 (2012).

[6]Y.-H. Chen, S. Varma, T. M. Antonsen, and H. M. Milchberg, Phys. Rev. Lett. **105**, 215005 (2010).

[7]M. Mlejnek, E. M. Wright, and J. V. Moloney, Opt. Lett. **23**, 382–384 (1998).

[8]S. Eisenmann, A. Pukhov, and A. Zigler, Phys. Rev. Lett. **98**, 155002 (2007).

[9]P. B. Corkum, C. Rolland, and T. Srinivasan-Rao, Phys. Rev. Lett. **57**, 2268 (1986); N. Zhavoronkov, Opt. Lett. **36**, 529 (2011).

[10]C. P. Hauri, R. B. Lopez-Martens, C. I. Blaga, K. D. Schultz, J. Cryan, R. Chirla, P. Colosimo, G. Doumy, A. M. March, C. Roedig, E. Sistrunk, J. Tate, J. Wheeler, L. F. DiMauro, and E. P. Power, Opt. Lett. **32**, 868 (2007); G. Stibenz, N. Zhavoronkov, and G. Steinmeyer, *ibid.* **31**, 274 (2006); B. Prade, M. Franco, A. Mysyrowicz, A. Couairon, H. Buersing,

B. Eberle, M. Krenz, D. Seiffer, and O. Vasseur, *ibid.* **31**, 2601 (2006); A. Couairon, J. Biegert, C. P. Hauri, W. Kornelisb, F. W. Helbingb, U. Keller, and A. Mysyrowicz, J. Mod. Opt. **53**, 75 (2006).

[11]J. Kasparian, M. Rodriguez, G. Méjean, J. Yu, E. Salmon, H. Wille, R. Bourayou, S. Frey, Y.-B. André, A. Mysyrowicz, R. Sauerbrey, J.-P. Wolf, and L. Wöste, Science **301**, 61 (2003).

[12]S. Tzortzakis, B. Prade, M. Franco, A. Mysyrowicz, S. Hüller, and P. Mora, Phys. Rev. E **64**, 057401 (2001).

[13]J.-C. Diels, R. Bernstein, K. Stahlkopf, and Xin Miao Zhao, Sci. Am. **277**, 50 (1997).

[14]S. Tzortzakis, B. Prade, M. Franco, and A. Mysyrowicz, Opt. Commun. **181**, 123 (2000).

[15]Y. Brelet, A. Houard, L. Arantchouk, B. Forestier, Y. Liu, B. Prade, J. Carbonnel, Y.-B. André, and A. Mysyrowicz, Appl. Phys. Lett. **100**, 181112 (2012).

[16]B. Forestier, A. Houard, I. Revel, M. Durand, Y. B. André, B. Prade, A. Jarnac, J. Carbonnel, M. Le Nevé, J. C. de Miscault, B. Esmiller, D. Chapuis, and A. Mysyrowicz, AIP Adv. **2**, 012151 (2012).

[17]K. Y. Kim, J. H. Glownia, A. J. Taylor, and G. Rodriguez, Opt. Express **15**, 4577 (2007).

[18]X. Lu and X.-C. Zhang, Phys. Rev. Lett. **108**, 123903 (2012).

[19]Y. Bai, L. Song, R. Xu, C. Li, P. Liu, Z. Zeng, Z. Zhang, H. Lu, R. Li, and Z. Xu, Phys. Rev. Lett. **108**, 255004 (2012).

[20]Y. S. You, T. I. Oh, and K. Y. Kim, Phys. Rev. Lett. **109**, 183902 (2012).

[21]A. Dogariu, J. B. Michael, M. O. Scully, and R. B. Miles, Science **331**, 442 (2011).

[22]P. Sprangle, J. Peñano, B. Hafizi, D. Gordon, and M. Scully, Appl. Phys. Lett. **98**, 211102 (2011); P. R. Hemmer, R. B. Miles, P. Polynkin, T. Siebert, A. V. Sokolov, P. Sprangle, and M. O. Scully, PNAS **108**, 3130 (2011).

[23]P. Polynkin, B. Pasenhow, N. Driscoll, M. Scheller, E. M. Wright, and J. V. Moloney, Phys. Rev. A **86**, 043410 (2012).

[24]D. Kartashov, S. Ališauskas, G. Andriukaitis, A. Pugžlys, M. Shneider, A. Zheltikov, S. L. Chin, and A. Baltuška, Phys. Rev. A **86**, 033831 (2012).

[25]J. H. Odhner, E. T. McCole, and R. J. Levis, J. Phys. Chem. A **115**, 13407 (2011).

[26]J. Odhner and R. J. Levis, Opt. Lett. **37**, 1775 (2012).

[27]A. Braun, G. Korn, X. Liu, D. Du, J. Squier, and G. Mourou, Opt. Lett. **20**, 73 (1995).

[28]D. Kartashov, S. Ališauskas, A. Pugžlys, A. Voronin, A. Zheltikov, M. Petrarca, P. Béjot, J. Kasparian, J.-P. Wolf, and A. Baltuška, Opt. Lett. **37**, 3456 (2012).

[29]T. Popmintchev, M.-C. Chen, D. Popmintchev, P. Arpin, S. Brown, S. Ališauskas, G. Andriukaitis, T. Balčiunas, O. D. Mücke, A. Pugžlys, A. Baltuška, B. Shim, S. E. Schrauth, A. Gaeta, C. Hernández-García, L. Plaja, A. Becker, A. Jaron-Becker, M. M. Murnane, and H. C. Kapteyn, Science **336**, 1287 (2012).

[30]J. P. Palastro, T. M. Antonsen, and H. M. Milchberg, Phys. Rev. A **86**, 033834 (2012); M. Kolesik and J. V. Moloney, Rep. Prog. Phys. **77**, 016401 (2014).

[31]K. Y. Kim, I. Alexeev, and H. M. Milchberg, Appl. Phys. Lett. **81**, 4124 (2002).

[32]Y.-H. Chen, S. Varma, I. Alexeev, and H. M. Milchberg, Opt. Express **15**, 7458 (2007).

[33]Y.-H. Chen, S. Varma, A. York, and H. M. Milchberg, Opt. Express **15**, 11341 (2007).

[34]S. P. Le Blanc, E. W. Gaul, N. H. Matlis, A. Rundquist, and M. C. Downer, Opt. Lett. **25**, 764 (2000).

[35]V. Loriot, E. Hertz, O. Faucher, and B. Lavorel, Opt. Express **17**, 13429 (2009).

[36]V. Loriot, P. Béjot, W. Ettoumi, Y. Petit, J. Kasparian, S. Henin, E. Hertz, B. Lavorel, O. Faucher, and J.-P. Wolf, Laser Phys. **21**, 1319 (2011).

[37]K. Hartinger and R. A. Bartels, Appl. Phys. Lett. **92**, 021126 (2008).

[38]J. K. Wahlstrand, Y.-H. Cheng, Y.-H. Chen, and H. M. Milchberg, Phys. Rev. Lett. **107**, 103901 (2011).

[39]A. Jarnac, G. Tamosauskas, D. Majus, A. Houard, A. Mysyrowicz, A. Couairon, and A.s Dubietis, Phys. Rev. A **89**, 033809 (2014).

[40]B. La Fontaine, F. Vidal, Z. Jiang, C. Y. Chien, D. Comtois, A. Desparois, T. W. Johnston, J.-C. Kieffer, H. Pépin, and H. P. Mercure, Phys. Plasmas **6**, 1615 (1999).

[41]F. Théberge, W. Liu, P. Tr. Simard, A. Becker, and S. L. Chin, "Plasma density inside a femtosecond laser filament in air: Strong dependence on external focusing," Phys. Rev. E **74**, 036406 (2006).

[42]G. Rodriguez, A. R. Valenzuela, B. Yellampalle, M. J. Schmitt, and K.-Y. Kim, J. Opt. Soc. Am. B **25**, 1988 (2008).

[43]R. P. Fischer, A. C. Ting, D. F. Gordon, R. F. Fernsler, G. P. DiComo, and P. Sprangle, IEEE Trans. Plasma Sci. **35**, 1430 (2007).

[44]T. R. Clark and H. M. Milchberg, Phys. Rev. Lett. **78**, 2373 (1997).

[45]S.-Y. Chen, G. S. Sarkisov, A. Maksimchuk, R. Wagner, and D. Umstadter, Phys. Rev. Lett. **80**, 2610 (1998).

[46]S. Varma, Y.-H. Chen, and H. M. Milchberg, Phys. Rev. Lett. **101**, 205001 (2008).

[47]C. H. Lin, J. P. Heritage, T. K. Gustafson, R. Y. Chiao, and J. P. McTague, Phys. Rev. A **13**, 813 (1976).

[48]W. Ettoumi, Y. Petit, J. Kasparian, and J.-P. Wolf, Opt. Express **18**, 6613 (2010).

[49]P. Béjot, E. Hertz, J. Kasparian, B. Lavorel, J.-P. Wolf, and O. Faucher, Phys. Rev. Lett. **106**, 243902 (2011).

[50]W. Ettoumi, P. Béjot, Y. Petit, V. Loriot, E. Hertz, O. Faucher, B. Lavorel, J. Kasparian, and J.-P. Wolf, Phys. Rev. A **82**, 033826 (2010).

[51]D. Novoa, H. Michinel, and D. Tommasini, Phys. Rev. Lett. **105**, 203904 (2010).

[52]M. Kolesik, E. M. Wright, and J. V. Moloney, Opt. Lett. **35**, 2550 (2010).

[53]J. Kasparian, P. Béjot, and J.-P. Wolf, Opt. Lett. **35**, 2795 (2010).

[54]P. Béjot and J. Kasparian, Opt. Lett. **36**, 4812 (2011).

[55]C. Bree, A. Demircan, and G. Steinmeyer, Phys. Rev. Lett. **106**, 183902 (2011).

[56]S. Varma, Y.-H. Chen, J. P. Palastro, A. B. Fallahkair, E. W. Rosenthal, T. Antonsen, and H. M. Milchberg, Phys. Rev. A **86**, 023850 (2012).

[57]J. P. Palastro, T. M. Antonsen, S. Varma, Y.-H. Chen, and H. M. Milchberg, Phys. Rev. A **85**, 043843 (2012).

[58]J. K. Wahlstrand and H. M. Milchberg, Opt. Lett. **36**, 3822 (2011).

[59]A. Dogariu, T. Xia, D. J. Hagan, A. A. Said, E. W. van Stryland, and N. Bloembergen, J. Opt. Soc. Am. B **14**, 796 (1997).

[60]J. K. Wahlstrand, J. H. Odhner, E. T. McCole, Y.-H. Cheng, J. P. Palastro, R. J. Levis, and H. M. Milchberg, Phys. Rev. A **87**, 053801 (2013).

[61]S. Zahedpour, J. K. Wahlstrand, and H. M. Milchberg, Phys. Rev. Lett. **112**, 143601 (2014).

[62]N. Jhajj, E. W. Rosenthal, R. Birnbaum, J. K. Wahlstrand, and H. M. Milchberg, Phys. Rev. X **4**, 011027 (2014).

[63]M. Scheller, M. S. Mills, M.-A. Miri, W. Cheng, J. V. Moloney, M. Kolesik, P. Polynkin, and D. N. Christodoulides, Nat. Photonics **8**, 297 (2014).

[64]Y.-H. Cheng, J. K. Wahlstrand, N. Jhajj, and H. M. Milchberg, Opt. Express **21**, 4740 (2013).

[65]N. Jhajj, Y.-H. Cheng, J. K. Wahlstrand, and H. M. Milchberg, Opt. Express **21**, 28980 (2013).

[66]J. K. Wahlstrand, N. Jhajj, E. W. Rosenthal, S. Zahedpour, and H. M. Milchberg, Opt. Lett. **39**, 1290 (2014).